CORA Cork Open Research Archive
Cartlann Taighde Oscailte Chorcaí

Title	Observational signatures of mass-loading in jets launched by rotating black holes
Authors	O'Riordan, Michael;Pe'er, Asaf;McKinney, Jonathan C.
Publication date	2018-01
Original Citation	O'Riordan, M., Pe'er, A. and McKinney, J. C. (2018) 'Observational Signatures of Mass-loading in Jets Launched by Rotating Black Holes', The Astrophysical Journal, 853(1), 44 (10 pp). doi:10.3847/1538-4357/aaa0c4
Type of publication	Article (peer-reviewed)
Link to publisher's version	http://stacks.iop.org/0004-637X/853/i=1/a=44 - 10.3847/1538-4357/aaa0c4
Rights	© 2018. The American Astronomical Society. All rights reserved
Download date	2024-05-04 05:08:36
Item downloaded from	https://hdl.handle.net/10468/5429

UCC
University College Cork, Ireland
Coláiste na hOllscoile Corcaigh

The Astrophysical Journal, 853:44 (10pp), 2018 January 20 https://doi.org/10.3847/1538-4357/aaa0c4
© 2018. The American Astronomical Society. All rights reserved.

Observational Signatures of Mass-loading in Jets Launched by Rotating Black Holes

Michael O' Riordan[1], Asaf Pe'er[1], and Jonathan C. McKinney[2]
[1] Physics Department, University College Cork, Cork, Ireland; michael_oriordan@umail.ucc.ie
[2] Department of Physics and Joint Space-Science Institute, University of Maryland, College Park, MD 20742, USA
Received 2017 November 13; revised 2017 November 27; accepted 2017 December 7; published 2018 January 22

Abstract

It is widely believed that relativistic jets in X-ray binaries (XRBs) and active-galactic nuclei are powered by the rotational energy of black holes. This idea is supported by general-relativistic magnetohydrodynamic (GRMHD) simulations of accreting black holes, which demonstrate efficient energy extraction via the Blandford–Znajek mechanism. However, due to uncertainties in the physics of mass loading, and the failure of GRMHD numerical schemes in the highly magnetized funnel region, the matter content of the jet remains poorly constrained. We investigate the observational signatures of mass loading in the funnel by performing general-relativistic radiative transfer calculations on a range of 3D GRMHD simulations of accreting black holes. We find significant observational differences between cases in which the funnel is empty and cases where the funnel is filled with plasma, particularly in the optical and X-ray bands. In the context of Sgr A*, current spectral data constrains the jet filling only if the black hole is rapidly rotating with $a \gtrsim 0.9$. In this case, the limits on the infrared flux disfavor a strong contribution from material in the funnel. We comment on the implications of our models for interpreting future Event Horizon Telescope observations. We also scale our models to stellar-mass black holes, and discuss their applicability to the low-luminosity state in XRBs.

Key words: accretion, accretion disks – black hole physics – galaxies: jets – Galaxy: center – radiative transfer – X-rays: binaries

1. Introduction

Relativistic jets are a ubiquitous phenomenon. They have been observed across a range of accreting black hole systems spanning more than 8 orders of magnitude in mass—from stellar-mass black holes in X-ray binaries (XRBs), to supermassive black holes in active galaxies. The Blandford–Znajek (BZ) process (Blandford & Znajek 1977), in which rotational energy is extracted electromagnetically from a Kerr black hole, is widely regarded as a plausible mechanism for driving these jets. In a force-free black hole magnetosphere, the BZ model predicts that energy is extracted from the black hole at a rate $P_{\rm BZ} = \kappa\, \Phi^2\, \Omega_{\rm H}^2\, /4\pi c$ (Blandford & Znajek 1977; Tchekhovskoy et al. 2010). Here, κ is a dimensionless number, which depends on the magnetic field geometry, Φ is the magnetic flux threading the horizon, $\Omega_H = ac/2r_{\rm H}$ is the angular velocity of the horizon, a is the dimensionless black hole spin, $r_{\rm H} = (1 + \sqrt{1 - a^2})r_g$ is the horizon radius, and $r_g = GM/c^2$ is the gravitational radius. The expected BZ jet power therefore depends strongly on the black hole spin, as well as the properties of the near-horizon magnetic field.

Sophisticated, global general-relativistic magnetohydrodynamic (GRMHD) simulations have largely confirmed the basic predictions of the BZ model. In particular, Tchekhovskoy et al. (2011) and McKinney et al. (2012) demonstrated jet-launching with efficiencies exceeding 100%, meaning that more energy flows out of the black hole than flows in. Such high efficiencies are only possible if enough ordered vertical magnetic flux can accumulate near the horizon. In this case, the magnetic pressure becomes comparable to the gas pressure, disrupting the inner accretion flow and forming a "magnetically arrested disk" (MAD; Narayan et al. 2003). By contrast, non-MAD flows (called SANE by Narayan et al. 2012) typically do not show very efficient energy extraction, even at high black hole spin, due to the turbulent, disordered fields at the horizon (McKinney & Blandford 2009).

In recent years, MAD and SANE GRMHD models have been used extensively to model Sgr A*, the extremely low-luminosity accreting supermassive black hole at the center of our Galaxy (Mościbrodzka et al. 2009, 2014; Shcherbakov et al. 2012; Mościbrodzka & Falcke 2013; Chan et al. 2015a, 2015b; Ball et al. 2016; Gold et al. 2017; Ressler et al. 2017). These studies have largely been motivated by very-long baseline interferometric observations with the Event Horizon Telescope (EHT; Doeleman et al. 2009a), which will soon resolve the structure in Sgr A* on spatial scales comparable to the Schwarzschild radius. The EHT will also resolve small-scale polarized structure, which carries information about the near-horizon magnetic field. Therefore, the EHT offers an unprecedented opportunity to test theories of accretion and jet-launching, and possibly even general relativity itself via measurements of the black hole shadow (e.g., Psaltis et al. 2015, and references therein).

Despite these important advances, significant theoretical uncertainties remain that hinder a direct comparison between the dynamical models and observations. In particular, there is considerable uncertainty in the mass-loading physics of BZ jets. It is well known that GRMHD codes fail inside the highly magnetized funnel (Gammie et al. 2003). This is because numerical errors accumulate when the ratio of the magnetic energy density to mass energy density becomes large. In what follows, we will refer to this ratio as the magnetization σ. To keep the numerical scheme stable, GRMHD codes typically inject matter when σ becomes larger than some (rather arbitrary) value. This effectively enforces a minimum density in the simulation, commonly referred to as a density floor. Although there are physical processes that may operate to mass-load the funnel, for example, pair cascades (Blandford & Znajek 1977; Levinson & Rieger 2011; Broderick &

Tchekhovskoy 2015) or photon annihilation (Mościbrodzka et al. 2011), the injection of floor material is arbitrary and chosen simply to avoid numerical issues. Therefore, the funnel mass and internal energy densities are not determined by the GRMHD simulations.

Although the injected floor material has little effect on the dynamics, it can affect the resulting spectra and so must be considered when comparing GRMHD models with observations. Depending on the choice of initialization for the floors, the plasma in the funnel might be tenuous enough such that it has a negligible contribution to the spectra. In this case, the jet emission is dominated by the funnel wall or "jet sheath" as in Mościbrodzka & Falcke (2013) and Mościbrodzka et al. (2014). This "empty funnel" situation can also be achieved by simply removing floor material from the funnel during the radiative transport calculation. The material to remove can be chosen in a number of ways, for example, as cells in a large bipolar cone (Shcherbakov & McKinney 2013), cells considered artificially hot or dense relative to their neighbors (Chan et al. 2015b), or cells with a large value of σ (O'Riordan et al. 2016a, 2016b).

Recently, Gold et al. (2017) argued that the prescription used for treating the funnel material could be very important when interpreting future observations from the EHT. In particular, they showed that the black hole shadow can be completely obscured in the case of significant emission from the funnel, while the absence of strong funnel emission can in fact mimic features of the shadow. Therefore, in order to test general relativity using EHT observations, it will be crucial to distinguish between features caused by strong-field gravity and those arising from the presence or absence of emitting matter in the jet.

In this work, we investigate the observational effects of mass loading in the regime, where the funnel remains force-free. That is, we restrict our analysis to the case where the funnel material is highly magnetized with $\sigma \gtrsim 10$. In the opposite regime, where the inertia of the funnel plasma cannot be neglected ($\sigma \lesssim 1$), Globus & Levinson (2013) showed that mass and energy loading of the field lines can strongly suppress or even switch off energy extraction from the black hole. This case would therefore involve significant modifications to the dynamical GRMHD models. We will study the observational consequences of this regime in a future work.

The structure of the paper is as follows. In Section 2, we briefly describe our GRMHD models, radiative transport code, and prescriptions for treating the electrons in the jet. In Section 3, we show the spectra from our GRMHD models and describe the observational effects of mass loading the funnel. In Section 4, we summarize and discuss out findings. Throughout the paper, we use units, where $G = c = 1$, which implies that the gravitational radius r_g and light-crossing time $t_g = r_g/c$ become $r_g = t_g = M$. We will occasionally reintroduce factors of c for clarity.

2. Models

2.1. GRMHD Simulations

We consider six MAD accretion flows from Tchekhovskoy et al. (2011) and McKinney et al. (2012), and a SANE accretion flow from McKinney & Blandford (2009). Five of our MAD models have a scale height of $H/R \approx 0.2$ and spins of $a = \{0.1, 0.2, 0.5, 0.9, 0.99\}$. These are called A0.1N100, A0.2N100, A0.5N100, A0.9N100, and A0.99N100 in McKinney et al. (2012). We will refer to these as our "thin-MAD" models. We also consider a very geometrically thick MAD model with $H/R \approx 1$ and a spin of $a = 0.9375$, called A0.94BfN40 in McKinney et al. (2012). We will refer to this model as "thick-MAD." Finally, we consider a SANE model with $H/R \approx 0.2$ and a spin of $a = 0.92$, called MB09D in McKinney et al. (2012).

In Figure 1, we show snapshots of our MAD and SANE models. The color shows the mass density and the black contours show the structure of the poloidal magnetic field (from the ϕ-integrated vector potential). The top panel shows the thin-MAD model with $a = 0.99$, the middle panel shows the thick-MAD model with $a = 0.9375$, and the bottom panel shows the SANE model with $a = 0.92$. The MAD models have large-scale, ordered poloidal fields in the disk and jet, while the disk in the SANE model has a more disordered field. In all models, we remove material from cells near the poles because coordinate singularities can cause numerical issues here. This is indicated as an excised region along the z-axis in Figure 1. Detailed descriptions of these models can be found in McKinney & Blandford (2009), Tchekhovskoy et al. (2011), McKinney et al. (2012), and O'Riordan et al. (2016a, 2016b).

2.2. Electron Temperature Prescription

We calculate the spectra from these models in a post-processing step using a general-relativistic radiative transport code based on `grmonty` (Dolence et al. 2009). We use snapshots from the GRMHD simulations as input, and include contributions to the spectra from synchrotron emission, absorption, and Compton scattering from relativistic thermal electrons. The mass accretion rates in our low-luminosity target applications of Sgr A* and the low/hard state in XRBs are expected to be well below the corresponding Eddington rate, which justifies treating the radiation in a post-processing step. The Eddington rate is defined as $\dot{M}_{\rm Edd}c^2 \equiv 10\,L_{\rm Edd} \approx 10^{39}\left(\frac{M}{M_\odot}\right)$ erg s^{-1} (Narayan & McClintock 2008). Since differences in mass density and magnetization can cause different heating and cooling rates for the protons and electrons in the disk and jet (e.g., Ressler et al. 2015; Foucart et al. 2016), we specify the proton-to-electron temperature ratio $\mathcal{T} \equiv T_p/T_e$ as a function of the plasma $\beta \equiv p_{\rm gas}/p_{\rm mag}$. Here, $p_{\rm gas}$ is the thermal pressure of the fluid, and $p_{\rm mag}$ is the magnetic pressure. In order to maximize the potential contributions from the highly magnetized funnel material, unless otherwise specified, we choose a critical value of $\beta_c = 0.2$ and set $\mathcal{T} = \mathcal{T}_{\rm disk} = 30$ in regions where $\beta > \beta_c$, and $\mathcal{T} = \mathcal{T}_{\rm jet} = 3$ in regions where $\beta \leqslant \beta_c$. For simplicity, we will refer to regions with $\beta \leqslant \beta_c$ as the "jet," and regions with $\beta > \beta_c$ as the "disk." In particular, the "jet" includes both the funnel wall and central funnel matter. Although the choice of β_c is somewhat arbitrary, we find that using $\beta_c = 0.2$ gives a reasonable distinction between the disk and jet, and our results are largely unaffected by small changes in β_c up to a factor of a few. We impose a smooth, exponential transition between the temperature ratios in the disk and jet by setting $\mathcal{T} = \mathcal{T}_{\rm jet}\, e^{-\beta/\beta_c} + \mathcal{T}_{\rm disk}(1 - e^{-\beta/\beta_c})$.

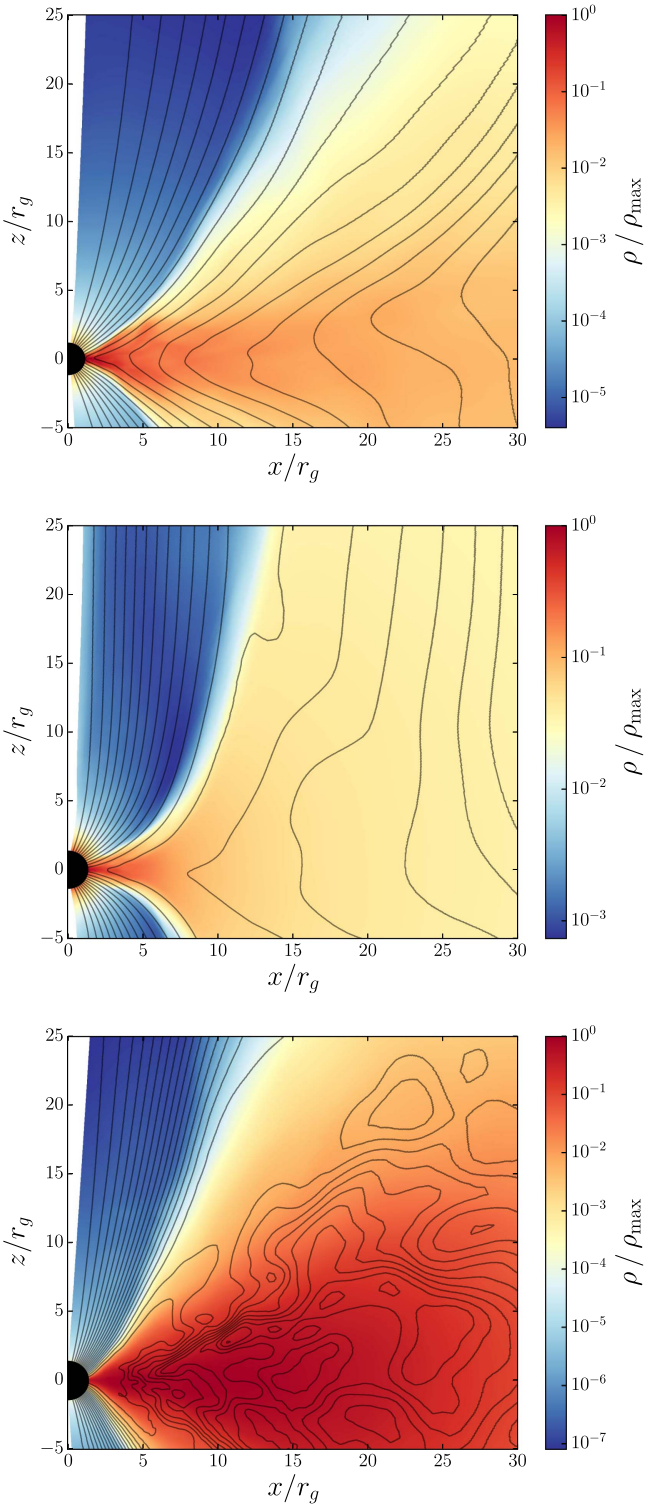

Figure 1. Snapshots of our MAD and SANE GRMHD models. The color shows the mass density and the poloidal magnetic field lines are represented by the black contours. The top panel shows the thin-MAD model with $H/R \approx 0.2$ and $a = 0.99$. The middle panel shows the thick-MAD model with $H/R \approx 1$ and $a = 0.9375$. The bottom panel shows the SANE model with $H/R \approx 0.2$ and $a = 0.92$. Both MAD models have large-scale ordered poloidal fields in the disk and jet. The white regions along the z-axis correspond to material that has been removed to avoid numerical issues due to coordinate singularities. The blue regions roughly correspond to the numerical density floors, which are removed in our "empty" funnel models (see the text for details about the floor removal).

2.3. Empty Funnel Prescription

To maintain numerical stability, GRMHD codes must inject material into the low-density, highly magnetized, funnel region. In particular, numerical errors accumulate when the magnetization becomes large $\sigma = b^2/\rho \gg 1$. Here, $b^2 = b^\mu b_\mu$, b^μ is the magnetic four-field, and ρ is the rest-mass density. The magnetic four-field can be written in terms of the lab-frame three-field B^i as $b^\mu = h^\mu_\nu B^\nu / u^t$, where u^μ is the fluid four-velocity and $h^\mu_\nu = \delta^\mu_\nu + u^\mu u_\nu$ is a projection tensor. In our units, the magnetic pressure is related to the magnetization by $p_{\rm mag} = \sigma\rho/2$. The injected floor material roughly corresponds to the blue regions in Figure 1. Although the injected numerical density floors do not affect the dynamics, they can be artificially hot and so might affect the resulting spectra. In O'Riordan et al. (2016a, 2016b), we considered the case where material from the central regions of the funnel does not contribute significantly to the observed spectrum. That is, we removed the floor material such that the middle of the funnel region was empty. In this work, we follow the same procedure for removing the floor material and will refer to the resulting models as "empty." For removing the floors, we set the density to zero in regions where $\sigma > \sigma_c(r)$. We use $\sigma_c = 20$ at the horizon, and linearly interpolate to $\sigma_c = 10$ at $r = 10\,r_g$. For larger radii, we use a fixed value of $\sigma_c = 10$. This ensures that the injected floors are removed, without removing material close to the black hole, which naturally becomes highly magnetized. Using this prescription, the center of the funnel region is removed, while the disk and funnel wall are not affected. The dashed lines in Figure 11, which we will refer to as the "edge" of the funnel wall, show the regions that are removed using this prescription.

2.4. Filled Funnel Prescription

We also consider the case where the funnel is mass-loaded and will refer to these models as "filled." When modeling the filled funnel, we restrict our attention to the regime in which the mass loading of the jet does not affect the magnetic field in the funnel. In covariant form, the energy and momentum exchange between an electromagnetic field and charged matter can be written as $\nabla_\mu T^{\mu\nu}_{\rm EM} = -F^{\mu\nu} j_\nu$, where ∇_μ is the covariant derivative, $T^{\mu\nu}_{\rm EM} = F^{\mu\alpha} F^\nu{}_\alpha - \frac{1}{4} g^{\mu\nu} F_{\alpha\beta} F^{\alpha\beta}$ is the electromagnetic stress-energy tensor, $F^{\mu\nu}$ is the electromagnetic field tensor, j^μ is the electric four-current density, and $g_{\mu\nu}$ is the metric. In the case where the plasma energy-momentum is many orders of magnitude less than that of the electromagnetic field, the energy and momentum exchange can be neglected. In this case, the electromagnetic stress-energy tensor is conserved by itself $\nabla_\mu T^{\mu\nu}_{\rm EM} = 0$. Such a situation is referred to as force-free because of the vanishing of the Lorentz four-force density $f^\mu = F^{\mu\nu} j_\nu$. The approximately force-free solution in the funnel will be preserved as long as the injected matter has $\sigma \gg 1$ (McKinney & Gammie 2004). In this regime, we can treat the funnel mass loading in a post-processing step. More significant mass loading with $\sigma \lesssim 1$ would affect the fluid dynamics and could even quench the BZ jet (Globus & Levinson 2013). In the case of a strongly mass-loaded funnel, the resulting GRMHD solution may deviate significantly from the models described here.

Various processes have been proposed that act to fill the funnel with electron–positron ($e^\pm$) or electron–proton (e–p) pairs; however, the physical mechanism that operates in nature to mass-load jets remains an open problem. GRMHD simulations

typically show the formation of a surface near the black hole that separates the inflowing and outflowing plasmas. This "stagnation" surface is continuously evacuated, resulting in large unscreened electric fields. Therefore, the stagnation surface might be the location of $e^{\pm}$ pair formation and subsequent acceleration (Levinson & Rieger 2011; Broderick & Tchekhovskoy 2015). Furthermore, depending on the radiation field produced by the inner regions of the accretion flow, the funnel might be filled with $e^{\pm}$ pairs via photon annihilation (Mościbrodzka et al. 2011). While these mechanisms both result in $e^{\pm}$ jets, there are also magnetohydrodynamic processes that might fill the jet with *e–p* pairs. These include magnetic Rayleigh–Taylor instabilities in the funnel wall (McKinney et al. 2012, and Appendix A), and magnetic field polarity inversions in the disk Dexter et al. (2014). Both of these processes inject matter from the disk into the center of the funnel. In this work, we do not specify a mass-loading mechanism, but instead consider the limiting cases of an empty funnel and a funnel filled with constant profiles of mass and internal energy density. We set the density and internal energy to be as large as possible, while still satisfying the force-free condition. Therefore, we expect the spectra from mass-loaded force-free jets to fall between the extremes considered here.

For our filled models, we first remove the floor material using the procedure described above, and then fill the empty funnel cells at each radius with constant mass and internal energy densities, equal to their corresponding values at the edge of the funnel wall (denoted by the dashed lines in Figure 11). We then rescale the material in the funnel and funnel wall to conserve energy. In practice, this re-scaling has little effect on the resulting spectra. Using this procedure, the properties of the plasma in the funnel are determined by the self-consistent material in the funnel wall. The resulting matter distribution in the funnel is in fact similar to the original floor material shown in Figure 1. However, we choose to manually fill the funnel to avoid any potential issues with artificially hot cells, which would otherwise have to be checked and removed as in Chan et al. (2015b). We show the mass and internal energy density distributions in our empty and filled models in Figure 11.

3. Results

3.1. Predictions for Spectra of Sgr A*

To scale our GRMHD models to Sgr A*, we set the black hole mass to be $M = 4 \times 10^6\, M_\odot$ (Gillessen et al. 2009) and adjust the mass accretion rate so that the resulting flux at 230 GHz is roughly consistent with the observational data. This emission likely originates from within a few Schwarzschild radii of the supermassive black hole (Doeleman et al. 2008), a region that is well resolved by the GRMHD simulations and has reached a quasi-steady state. In Figure 2, we show spectra from the thin-MAD model with a black hole spin of $a = 0.1$, for two different observer inclinations of $\theta = \pi/2$ (perpendicular to the spin axis), and $\theta = \pi/3$. The "empty" model corresponds to the case where the funnel material does not contribute significantly to the observed spectra. In this case, we have removed all the plasma from the center of the funnel and so the emission originates in the accretion disk and in the funnel wall. The "filled" model corresponds to the extreme case where the funnel is filled with constant profiles of mass and internal energy densities. The values are chosen to be equal to those at the edge of the funnel wall.

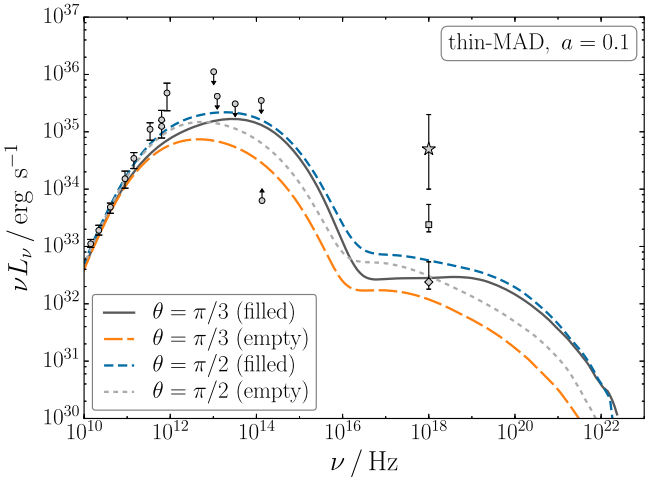

Figure 2. Comparison of the spectra for the empty and filled funnel thin-MAD models with $a = 0.1$. The radio data points and IR limits are the same as those considered by Chan et al. (2015b). The X-ray flux during quiescence is marked by the square data point (Baganoff et al. 2003), while the diamond marks 10% of the quiescent X-ray flux (Neilsen et al. 2013). The range of observed X-ray flares is represented by the star Neilsen et al. (2013). The radio emission originates in the funnel wall and so is not sensitive to the mass loading of the funnel. The funnel material primarily contributes to the IR and optical bands, with a corresponding increase in the synchrotron self-Compton component. In this low-spin case, both the empty and filled funnel models are largely consistent with the data.

The radio data points and IR limits are the same as those considered by Chan et al. (2015b). In particular, the IR limits represent the highest and lowest observed fluxes. The X-ray flux during quiescence is marked by the square data point (Baganoff et al. 2003). The diamond marks 10% of the quiescent X-ray flux, which is the estimated contribution from the inner accretion flow (Neilsen et al. 2013). The range of observed X-ray flares is represented by the star and corresponding error bars (Neilsen et al. 2013).

The mass accretion rate in Figure 2 is set such that the average rate at the horizon is $\dot{M} \approx 10^{-7}\, \dot{M}_{\rm Edd}$. Interestingly, the radio emission at frequencies $\nu \lesssim 10^{12}$ Hz is not sensitive to the mass loading of the funnel. This is because this emission is dominated by the funnel wall. This is consistent with the findings of Mościbrodzka et al. (2014), who refer to this region as the "jet sheath." Although there is a clear increase at IR and optical frequencies relative to the empty funnel case, both the empty and filled funnel models are largely consistent with the data.

In Figure 3, we show the spectra for the higher-spin case of $a = 0.5$. The spectra are qualitatively similar to those in Figure 2; however, the enhancement at IR and optical frequencies is larger. To obtain better fits with the filled model, we reduced the accretion rate by a factor of $\sim$1.5 in the bottom panel relative to the top panel. The increase in this synchrotron component causes a corresponding increase in synchrotron self-Compton emission in the hard X-rays. As with the $a = 0.1$ model, both the empty and filled funnel cases fit the data reasonably well; however, the IR flux in the filled model is very close to the upper limits on the observed flux.

In Figure 4, we show the thin-MAD model with $a = 0.9$. The IR and X-ray limits clearly disfavor the case where the funnel material contributes significantly to the emission. Although the X-ray and IR emission can be brought within the limits by adjusting the mass accretion rate, this would also significantly reduce the radio flux, which originates in the

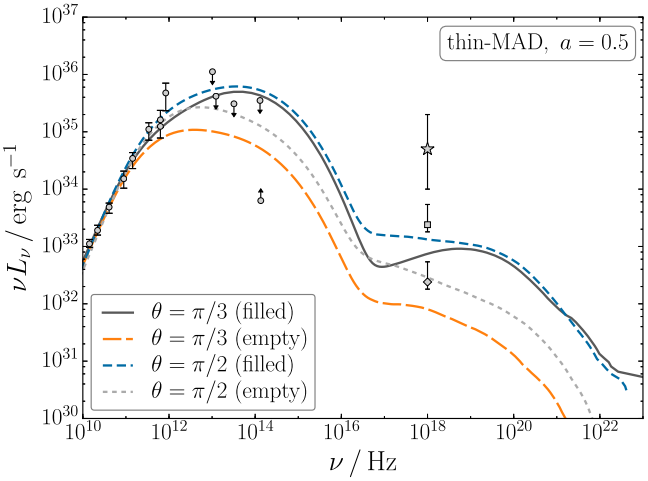

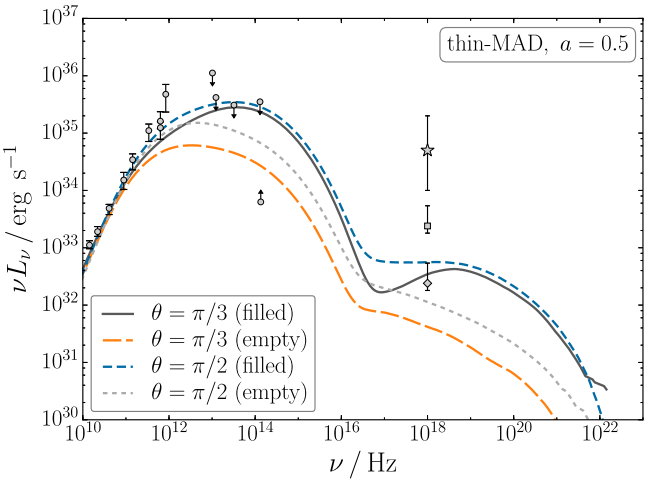

Figure 3. Spectra for the thin-MAD model with $a = 0.5$. The spectra are qualitatively similar to the $a = 0.1$ case, but with a larger contribution from the funnel material. To obtain better fits with the filled model, the accretion rate in the bottom panel has been decreased by a factor of ∼1.5 relative to that in the top panel. Although both the empty and filled funnel models are consistent with the data, the IR emission in the filled funnel case is close to the maximum flux allowed by observations.

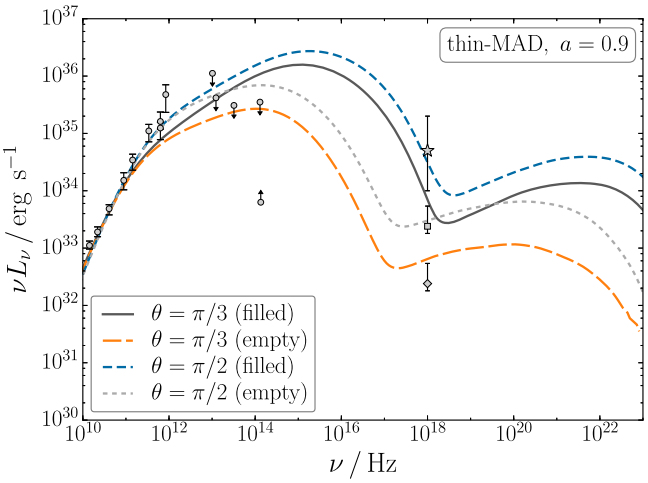

Figure 4. Spectra for the thin-MAD model with $a = 0.9$. In this case, the IR limits and X-ray estimates disfavor a filled funnel component. Even the empty funnel case is approaching the limits of the observations. While a lower accretion rate would decrease the IR and X-ray flux toward values more consistent with the data, the radio flux would then be missed by a large amount.

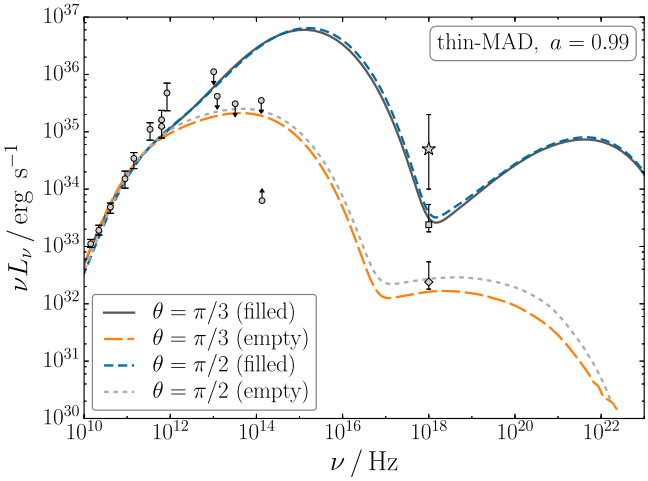

Figure 5. Spectra for the thin-MAD model with $a = 0.99$. As with the $a = 0.9$ case, the IR and X-ray data disfavor the filled funnel model. Furthermore, fitting the empty funnel model to the data requires suppressing the emission from close to the horizon by increasing the proton-to-electron temperature ratio of the inflowing material.

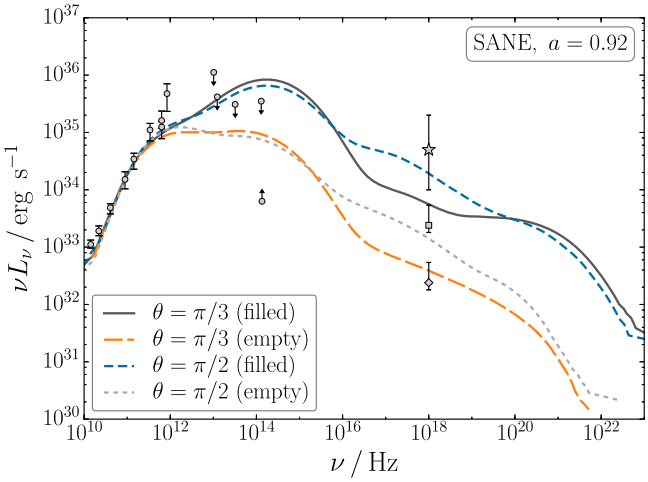

Figure 6. Spectra for the SANE model with $a = 0.92$. As in the high-spin MAD models, the IR limits disfavor models with strong funnel emission.

funnel wall and is independent of the mass loading. The difference between the empty and filled models is even more dramatic in the extreme $a = 0.99$ case, which we show in Figure 5. As discussed in O'Riordan et al. (2016a), the emission from this model is strongly dominated by the near-horizon plasma. In order to give reasonable fits to the data, even in the empty funnel case, we suppressed this near-horizon radiation by imposing a temperature ratio of $\mathcal{T} = 300$ on the inflowing material. A similar result was found by Chan et al. (2015b), whose best-fit MAD models have very large proton-to-electron temperature ratios in the disk.

In Figure 6, we show the spectra calculated from our SANE model with $a = 0.92$ and a mass accretion rate of $\dot{M} \approx 10^{-6}\dot{M}_{\rm Edd}$. This model has the same scale height of $H/R \approx 0.2$ as our thin-MAD models. As in the thin-MAD case, the radio emission is insensitive to the mass loading of the funnel. The higher mass accretion rate results in a larger optical depth, which is clearly reflected in the high-energy parts of the spectra that show multiple Compton scatterings. Interestingly, as in the high-spin MAD models, the filled funnel model

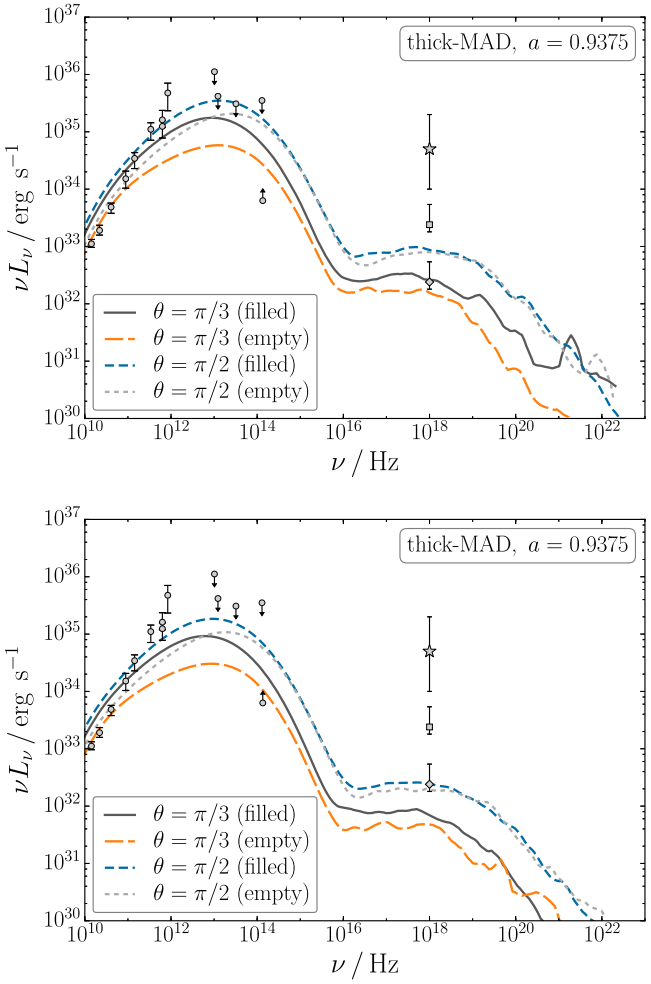

Figure 7. Spectra for the geometrically thick ($H/R \approx 1$) MAD model with $a = 0.9375$. The accretion rate in the top panel is larger than that in the bottom panel by a factor of ~1.5. This model gives a poorer fit to the radio data than the geometrically thinner models. In this case, although the black hole is rotating rapidly, both the empty and filled models provide reasonably similar fits to the data. This is because the funnel emission is somewhat suppressed relative to the other models and so the difference between empty and filled funnels is less extreme.

significantly overproduces IR emission and so an empty funnel is favored by the data.

To conclude, for all our thin-MAD models and our SANE model, we find that the radio flux is dominated by the funnel wall and is largely independent of the mass loading of the jet. We also find a significantly larger IR flux in the filled models than in the empty models. From this, we expect that the ratio of the IR flux and 230 GHz flux could be used as a probe of mass-loading processes in the funnel. Furthermore, in the context of Sgr A*, although our low-spin models are consistent with the data in both empty and filled funnel cases, the higher-spin models only fit the data provided the funnel material does not contribute significantly to the observed spectrum.

In Figure 7, we show the spectra calculated from our thick-MAD model, which has a black hole spin of $a = 0.9375$ and a very geometrically thick disk ($H/R \approx 1$). As in Figure 3, the accretion rate in the bottom panel is ~1.5 times lower than that in the top panel. Although the emission from our thin-MAD and SANE models is dominated by the region $r \lesssim 30\,M$, which has reached a quasi-steady state, the outer radii of our thick-MAD model can contribute significantly to the emission. The outer radii of our GRMHD models have not had enough time to reach a steady state and so the plasma properties depend strongly on the initial conditions in the torus. Furthermore, the 230 GHz flux, which we have been using to normalize our models likely originates in the inner few r_g of the accretion flow (Doeleman et al. 2008). Therefore, we follow the procedure of Shcherbakov et al. (2012) to analytically extend the fluid quantities to large radii. We extend the fluid properties at $r = 30\,M$ as power laws out to the Bondi radius in order to match the estimated density and temperature for Sgr A* at this radius. We further assume an isothermal jet with electron temperature $\Theta = kT/mc^2 = 50$ (Mościbrodzka et al. 2014; Chan et al. 2015b; Gold et al. 2017), which provides a better fit to the radio emission than a constant temperature ratio for this model. The difference between the empty and filled funnel models is smaller than in the high-spin thin-MAD and SANE cases and so both provide similar fits to the data. Contrary to the previous cases, the funnel filling primarily affects the lower-frequency emission. This is consistent with Gold et al. (2017), who found that the 230 GHz images of their models were affected by the funnel filling. We will perform a more thorough investigation of the dependence on the disk scale height and prescriptions for extending the data to the Bondi radius in a future work.

3.2. Predictions for Spectra of the Low/Hard State in XRBs

In this section, we scale our thin-MAD models to the low-luminosity state in XRBs by setting the black hole mass to $M = 10\,M_\odot$. For comparing the different GRMHD models, we fix the mass accretion rate to be $\dot{M} \approx 10^{-6}\,\dot{M}_{\rm Edd}$. To maximize the potential effects of the funnel emission, we again consider the case where the proton-to-electron temperature ratios in the disk and jet are $\mathcal{T}_{\rm disk} = 30$ and $\mathcal{T}_{\rm jet} = 3$.

In Figure 8, we show the spectra for the low-spin models with $a = 0.1$ and $a = 0.5$. The results are qualitatively similar to the corresponding spectra for Sgr A*, with differences in the peak frequencies and overall luminosity due to changes in the black hole mass and accretion rate. In particular, we find that the filled funnel models show enhanced hard UV/soft X-ray emission, while the optical and lower-frequency fluxes are unaffected by the mass loading.

In Figure 9, we show the spectra for the high-spin models with $a = 0.9$ and $a = 0.99$. We find very large differences between the empty and filled funnel models, with the funnel contribution shifting to higher frequencies. In this case, the X-rays and γ-rays are significantly modified by the funnel matter, while frequencies below $\sim 10^{16}$ Hz are unaffected by the funnel contribution. In the $a = 0.99$ case, the radiative efficiency is large, approaching values $\gtrsim 10\%$, especially in the filled funnel model. A similar result was reported by Ryan et al. (2017), who found that accretion flows with $a = 0.5$ can approach 1% radiative efficiency by $\dot{M} \sim 10^{-5}\dot{M}_{\rm Edd}$. To avoid complications due to radiative cooling, we investigate a lower accretion rate of $\dot{M} \approx 10^{-7}\dot{M}_{\rm Edd}$, and show the resulting spectra in Figure 10. The spectra in the hard X-rays and below are qualitatively similar to those in Figure 9, and so our conclusions about the effects of the funnel mass loading still hold. This is not surprising since, as shown in Appendix B, although the luminosity depends very strongly on the accretion rate $L_{\rm syn} \sim \dot{M}^2$, the frequency depends only weakly on $\dot{M}$ as $\nu_{\rm syn} \sim \dot{M}^{1/2}$. There is a larger difference in the synchrotron self-Compton component due to the linear dependence of the Compton y parameter on $\dot{M}$ (see Appendix B).

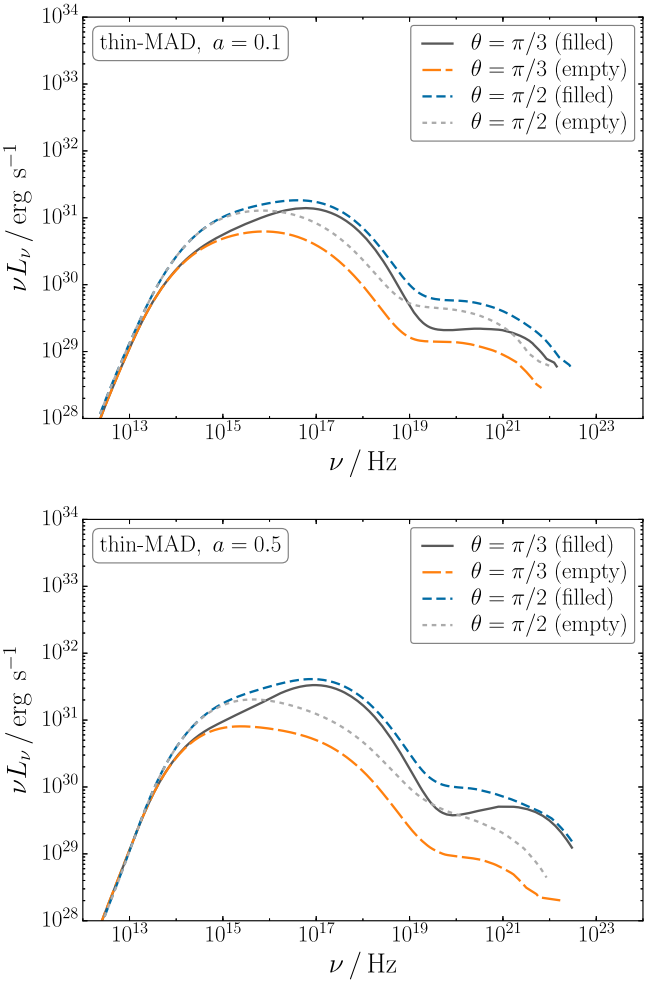

Figure 8. Spectra for thin-MAD models with $a = 0.1$ (top) and $a = 0.5$ (bottom). The black hole mass has been set to $M = 10\,M_\odot$. The spectra are qualitatively similar to the results for Sgr A*. The optical and lower-frequency emission is insensitive to the funnel material, while the hard UV and soft X-rays are significantly enhanced relative to the empty funnel case.

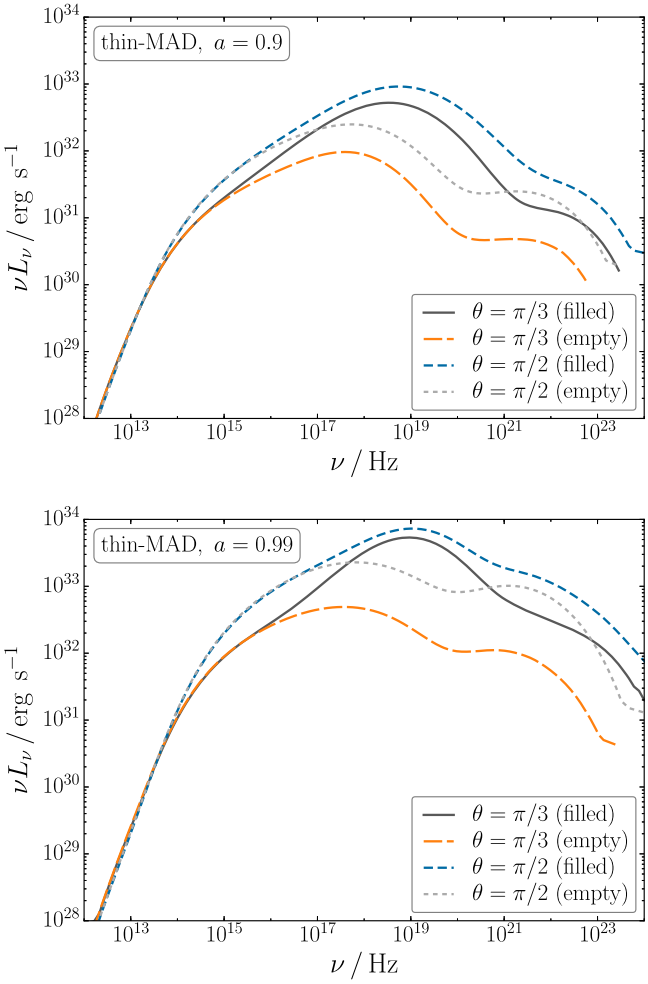

Figure 9. Spectra for the thin-MAD models with $a = 0.9$ (top) and $a = 0.99$ (bottom). The X-ray flux is significantly higher in the filled funnel models, while emission at frequencies $\lesssim 10^{16}$ Hz is unaffected by the funnel matter.

4. Summary and Discussion

In this work, we investigated the observational effects of mass loading in BZ jets. We considered the case in which the plasma in the funnel remains force-free, which allowed us to treat the mass loading in a post-processing step. We found significant differences between models with an empty funnel and models where the funnel was filled with highly magnetized plasma. In particular, in the context of Sgr A* the IR and optical flux is enhanced relative to the empty funnel case. Interestingly, the radio emission from our thin-MAD and SANE models is dominated by the funnel wall and so is largely unaffected by the mass loading. We identify the ratio of the IR and 230 GHz flux as a potential observational probe of the filling factor of the funnel.

As argued by Gold et al. (2017), understanding the contribution from the funnel material will be extremely important for interpreting future EHT observations of the black hole shadow in Sgr A*. They showed that the absence of significant 230 GHz emission from the funnel can appear as a "hole" in the images, mimicking features of the black hole shadow. Since the radio emission from our models is not affected by the funnel material, we expect that the mass loading of the BZ jet will not have a large impact on images from the EHT (unless the disk is very thick with $H/R \sim 1$, as shown in Figure 7). This means that even mass-loaded BZ jets may appear as "holes" in images from the EHT.

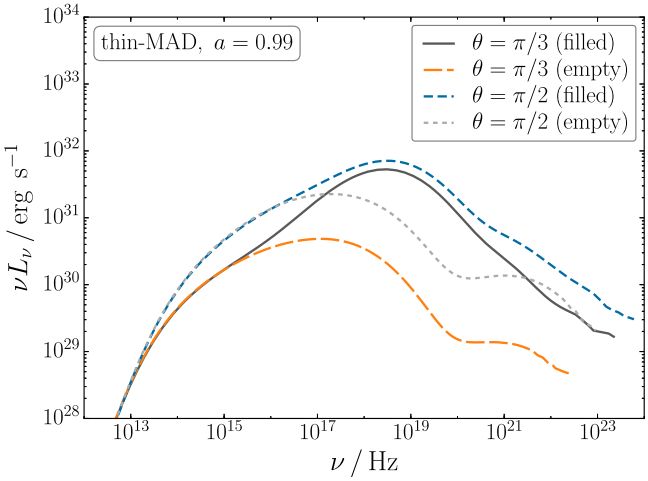

Figure 10. Same as the bottom panel of Figure 9, but with a lower accretion rate of $\dot{M} \approx 10^{-7}\dot{M}_{\rm Edd}$. Although the luminosity is significantly lower than in the previous case, the frequencies at which the emission is enhanced are similar. This is due to the reasonably weak dependence of the frequency on the accretion rate.

We find qualitatively similar results in the context of XRBs, although shifted to higher frequencies due to changes in the black hole mass and accretion rate. It is often argued that inverse Compton emission from a corona of hot electrons surrounding the inner accretion flow is responsible for the X-ray emission observed in XRBs (e.g., Titarchuk 1994; Magdziarz & Zdziarski 1995; Esin et al. 1997, 2001; Gierlinski et al. 1997; Poutanen 1998; Cadolle Bel et al. 2006; Yuan et al. 2007; Narayan & McClintock 2008; Niedźwiecki et al. 2012, 2014; Qiao & Liu 2015). However, there is significant degeneracy between these models and ones in which a large fraction of the X-ray emission originates in the base of the jet (e.g., Mirabel & Rodríguez 1994; Markoff et al. 2001, 2003, 2005, 2015; Falcke et al. 2004; Bosch-Ramon et al. 2006; Gupta et al. 2006; Kaiser 2006; Kylafis et al. 2008; Maitra et al. 2009; Pe'er & Casella 2009; Pe'er & Markoff 2012; O'Riordan et al. 2016b). Understanding the funnel mass loading could be crucial for breaking this degeneracy and constraining the role of the jet in producing the observed high-energy X-ray emission in the low/hard state.

Our results have interesting implications for explaining the scatter in the fundamental plane of black hole activity (Merloni et al. 2003; Falcke et al. 2004). The fundamental plane is an empirical correlation between black hole mass, radio luminosity, and X-ray luminosity, which spans the mass scale from XRBs to active galaxies. This correlation suggests that low-luminosity accreting black hole systems are scale invariant. Our results imply that differences in the jet mass loading could contribute to the scatter about the best-fit correlation. In particular, at high black hole spin, the X-ray emission can vary by more than two orders of magnitude between the empty and filled models, while the radio emission remains constant. Therefore, in addition to variations in quantities such as the mass accretion rate, black hole spin, and viewing angle, the mass loading of the jet could play a significant role in producing the observed scatter.

For our empty funnel models, we set the plasma density in the funnel to zero. However, this case represents a wider class of models in which the funnel contains material that does not contribute significantly to the emission. For example, models in which the proton-to-electron temperature ratio in the jet is comparable to that in the disk result in similar spectra to the empty funnel cases. This is because the denser funnel wall dominates the jet component unless the plasma in the center of the funnel is hot enough. For similar assumptions about the electron temperatures, the spectra from more complicated matter profiles in force-free jets should fall within the limits considered here. In a future work, we will investigate observational signatures of the regime where the force-free approximation breaks down. As shown by Globus & Levinson (2013), in this case, the solution in the funnel can deviate significantly from the BZ funnel solutions in our dynamical models.

We have not specified a mass-loading mechanism, but have simply compared spectra from the empty funnel case to the extreme case of a steady, force-free funnel with constant mass and internal energy density profiles. As well as spectral properties, we expect that variability studies will play a key role in constraining the mass-loading physics systems such as Sgr A*. Importantly, many of the proposed mass-loading mechanisms operate on very different timescales, and so could, in principle, be distinguished by the EHT. For example, pair production by vacuum gaps in the black hole magnetosphere is expected to be intermittent, and vary on timescales comparable to the light-crossing time of the black hole (Levinson & Rieger 2011; Broderick & Tchekhovskoy 2015). This timescale is extremely short in Sgr A*, roughly equal to one minute. However, it might be possible with the EHT to study structures in the accretion flow that vary on minute timescales (Doeleman et al. 2009a, 2009b). This could provide valuable constraints on the physics of near-horizon mass loading. Other mass-loading processes may operate on timescales significantly longer than the light-crossing time. For example, pairs may be produced by photon annihilation (Mościbrodzka et al. 2011) on timescales determined by radiation field of the disk. Furthermore, magnetohydrodynamic processes such as magnetic Rayleigh–Taylor instabilities in the funnel wall (McKinney et al. 2012, and Appendix A), or magnetic field polarity inversions in the disk Dexter et al. (2014) can inject matter from the disk into the center of the funnel. These processes operate on spatial scales much larger than the Schwarzschild radius, and so the corresponding variability could be resolved by future observations.

A significant limitation of the current work is our simplified treatment of the emitting electrons. In particular, we neglect the contribution from nonthermal electrons which might be present due to acceleration by shock waves (e.g., Sironi et al. 2015), magnetic reconnection (e.g., Sironi & Spitkovsky 2014), or due to the injection process itself (e.g., Levinson & Rieger 2011). Although these nonthermal electrons would likely affect the high-frequency emission in our spectra, including these processes would introduce additional poorly constrained free parameters into our models, and so we neglect this contribution as a first step. We also use a simple prescription for calculating the electron temperature by varying the proton-to-electron temperature ratio as a function of the plasma β. This ratio is a free parameter that is poorly constrained both by theory and observations. We choose values consistent with the findings of recent, sophisticated models of the electron thermodynamics in collisionless accretion flows (Ressler et al. 2015; Foucart et al. 2016; Sądowski et al. 2017), which show that the electron temperature is comparable to the proton temperature in highly magnetized regions of the flow. Modeling the electron physics in accretion disks and jets remains an active area of research, which will hopefully be informed further by upcoming observations with the EHT.

The authors thank Alexander Tchekhovskoy for providing simulation data. A.P. and M.O.R. acknowledge the DJEI/DES/SFI/HEA Irish Centre for High-End Computing (ICHEC) for the provision of computational facilities under project ucast008b. M.O.R. is supported by the Irish Research Council under grant number GOIPG/2013/315. This research was partially supported by the European Union Seventh Framework Programme (FP7/2007-2013) under grant agreement no 618499. J.C.M. acknowledges NASA/NSF/TCAN (NNX14AB46G), NSF/XSEDE/TACC (TGPHY120005), and NASA/Pleiades (SMD-14-5451). The authors would like to thank the anonymous referee for constructive comments, which have improved the quality of the manuscript.

Software: `HARM` (Gammie et al. 2003), `grmonty` (Dolence et al. 2009).

Appendix A
Mass and Internal Energy Densities in MAD and SANE GRMHD Models

In Figure 11, we show (ϕ-averaged) snapshots of our MAD and SANE GRMHD models. The left panels show the mass density, and the right panels show the internal energy density. As in Figure 1, the top panel shows the thin-MAD model with

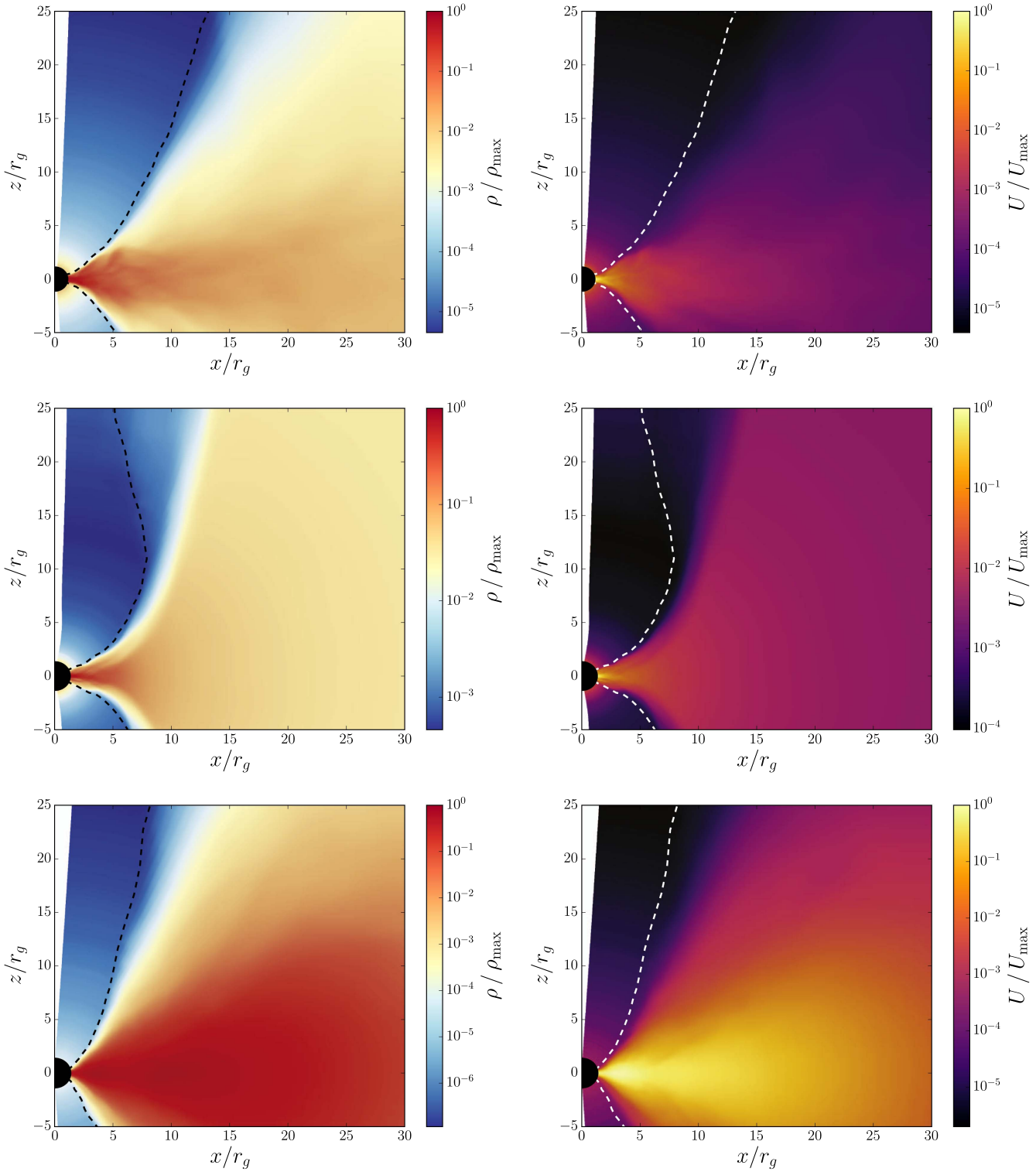

Figure 11. Snapshots of our MAD and SANE GRMHD models. The left panels show the mass density, and the right panels show the internal energy density. The top panel shows the thin-MAD model with $H/R \approx 0.2$ and $a = 0.99$. The middle panel shows the thick-MAD model with $H/R \approx 1$ and $a = 0.9375$. The bottom panel shows the SANE model with $H/R \approx 0.2$ and $a = 0.92$. The funnel regions are manually filled with constant profiles of mass and internal energy densities, according to the prescription described in Section 2. The dashed lines represent the region that is removed in the "empty" funnel models. In the text, we refer to the surface represented by the dashed lines as the "edge" of the funnel wall.

$H/R \approx 0.2$ and $a = 0.99$, the middle panel shows the thick-MAD model with $H/R \approx 1$ and $a = 0.9375$, and the bottom panel shows the SANE model with $H/R \approx 0.2$ and $a = 0.92$. In these plots, the funnel regions have been filled with constant profiles of mass and internal energy according to the prescription described in Section 2. The dashed lines represent the regions affected by the numerical floor material (prior to the manual filling of the funnel), which are removed in the "empty" funnel models. The jet in the thick-MAD model (middle panel) has a region near $r \approx 20\, r_g$ that is not affected by the numerical

density floors. Instead, this is material that has moved from the disk into the funnel due to instabilities at the jet-disk interface (McKinney et al. 2012). This is a transient feature, which has little effect on the spectra in this case. However, such disk-jet instabilities are a possible physical mechanism for mass loading the jet.

Appendix B
Dependence of the Spectra on the Black Hole Mass and Mass Accretion Rate

The synchrotron luminosity scales with the fluid properties as $L_{\rm syn} \sim \rho B^2 \Theta^2 V$, where ρ is the mass density, B is the magnetic field strength, $\Theta = kT/mc^2$ is the electron temperature, and V is the volume of the emitting region. The mass density scales with the black hole mass and accretion rate as $\rho \sim \dot{M} t_g/V \sim \dot{M}/M^2$, where we have used that $t_g = r_g/c \sim M$ and $V \sim M^3$. The magnetic energy density scales in the same way. Since we are neglecting radiation pressure, the electron temperature is simply proportional to the ratio of the internal and mass energy densities and so is independent of M and $\dot{M}$. Therefore, the luminosity scales as $L_{\rm syn} \sim \dot{M}^2/M$. It is convenient to write the accretion rate as a fraction η of the Eddington rate $\dot{M}_{\rm Edd}$. Since $\dot{M}_{\rm Edd}$ is proportional to the black hole mass, we find that $\rho \sim \eta/M$ and so $L_{\rm syn} \sim \eta^2 M$. We can follow the same procedure to find scalings for the synchrotron frequency $\nu_{\rm syn} \sim B\Theta^2 \sim \sqrt{\eta/M}$, the optical depth $\tau = n\sigma_T R \sim \eta$, and the Compton y parameter $y = 16\Theta^2\tau \sim \eta$ (Rybicki & Lightman 1979). We conclude that the luminosities of the synchrotron and Compton spectral components depend strongly on the mass accretion rate as $L_{\rm syn} \sim \dot{M}^2$ and $L_{\rm Compton} = yL_{\rm syn} \sim \dot{M}^3$, while the frequencies of these components depend only weakly on $\dot{M}$ as $\nu_{\rm syn} \sim \dot{M}^{1/2}$ and $\nu_{\rm Compton} \sim \Theta^2 \nu_{\rm syn} \sim \dot{M}^{1/2}$. Although we have neglected synchrotron self-absorption in these simple analytic scalings, we include this process in our numerical calculations of the spectra.

ORCID iDs

Michael O' Riordan https://orcid.org/0000-0002-0540-208X
Asaf Pe'er https://orcid.org/0000-0001-8667-0889
Jonathan C. McKinney https://orcid.org/0000-0002-9222-599X

References

Baganoff, F. K., Maeda, Y., Morris, M., et al. 2003, ApJ, 591, 891
Ball, D., Özel, F., Psaltis, D., & Chan, C.-K. 2016, ApJ, 826, 77
Blandford, R. D., & Znajek, R. L. 1977, MNRAS, 179, 433
Bosch-Ramon, V., Romero, G. E., & Paredes, J. M. 2006, A&A, 447, 263
Broderick, A. E., & Tchekhovskoy, A. 2015, ApJ, 809, 97
Cadolle Bel, M., Sizun, P., Goldwurm, A., et al. 2006, A&A, 446, 591
Chan, C.-K., Psaltis, D., Özel, F., et al. 2015a, ApJ, 812, 103
Chan, C.-K., Psaltis, D., Özel, F., Narayan, R., & Sądowski, A. 2015b, ApJ, 799, 1
Dexter, J., McKinney, J. C., Markoff, S., & Tchekhovskoy, A. 2014, MNRAS, 440, 2185
Doeleman, S., Agol, E., Backer, D., et al. 2009a, in Astronomy, Vol. 2010, astro2010: The Astronomy and Astrophysics Decadal Survey, 68
Doeleman, S. S., Fish, V. L., Broderick, A. E., Loeb, A., & Rogers, A. E. E. 2009b, ApJ, 695, 59
Doeleman, S. S., Weintroub, J., Rogers, A. E. E., et al. 2008, Natur, 455, 78
Dolence, J. C., Gammie, C. F., Mościbrodzka, M., & Leung, P. K. 2009, ApJS, 184, 387
Esin, A. A., McClintock, J. E., Drake, J. J., et al. 2001, ApJ, 555, 483
Esin, A. A., McClintock, J. E., & Narayan, R. 1997, ApJ, 489, 865
Falcke, H., Körding, E., & Markoff, S. 2004, A&A, 414, 895
Foucart, F., Chandra, M., Gammie, C. F., & Quataert, E. 2016, MNRAS, 456, 1332
Gammie, C. F., McKinney, J. C., & Tóth, G. 2003, ApJ, 589, 444
Gierlinski, M., Zdziarski, A. A., Done, C., et al. 1997, MNRAS, 288, 958
Gillessen, S., Eisenhauer, F., Trippe, S., et al. 2009, ApJ, 692, 1075
Globus, N., & Levinson, A. 2013, PhRvD, 88, 084046
Gold, R., McKinney, J. C., Johnson, M. D., & Doeleman, S. S. 2017, ApJ, 837, 180
Gupta, S., Böttcher, M., & Dermer, C. D. 2006, ApJ, 644, 409
Kaiser, C. R. 2006, MNRAS, 367, 1083
Kylafis, N. D., Papadakis, I. E., Reig, P., Giannios, D., & Pooley, G. G. 2008, A&A, 489, 481
Levinson, A., & Rieger, F. 2011, ApJ, 730, 123
Magdziarz, P., & Zdziarski, A. A. 1995, MNRAS, 273, 837
Maitra, D., Markoff, S., Brocksopp, C., et al. 2009, MNRAS, 398, 1638
Markoff, S., Falcke, H., & Fender, R. 2001, A&A, 372, L25
Markoff, S., Nowak, M., Corbel, S., Fender, R., & Falcke, H. 2003, A&A, 397, 645
Markoff, S., Nowak, M. A., Gallo, E., et al. 2015, ApJL, 812, L25
Markoff, S., Nowak, M. A., & Wilms, J. 2005, ApJ, 635, 1203
McKinney, J. C., & Blandford, R. D. 2009, MNRAS, 394, L126
McKinney, J. C., & Gammie, C. F. 2004, ApJ, 611, 977
McKinney, J. C., Tchekhovskoy, A., & Blandford, R. D. 2012, MNRAS, 423, 3083
Merloni, A., Heinz, S., & di Matteo, T. 2003, MNRAS, 345, 1057
Mirabel, I. F., & Rodríguez, L. F. 1994, Natur, 371, 46
Mościbrodzka, M., & Falcke, H. 2013, A&A, 559, L3
Mościbrodzka, M., Falcke, H., Shiokawa, H., & Gammie, C. F. 2014, A&A, 570, A7
Mościbrodzka, M., Gammie, C. F., Dolence, J. C., & Shiokawa, H. 2011, ApJ, 735, 9
Mościbrodzka, M., Gammie, C. F., Dolence, J. C., Shiokawa, H., & Leung, P. K. 2009, ApJ, 706, 497
Narayan, R., Igumenshchev, I. V., & Abramowicz, M. A. 2003, PASJ, 55, L69
Narayan, R., & McClintock, J. E. 2008, NewAR, 51, 733
Narayan, R., Sadowski, A., Penna, R. F., & Kulkarni, A. K. 2012, MNRAS, 426, 3241
Neilsen, J., Nowak, M. A., Gammie, C., et al. 2013, ApJ, 774, 42
Niedźwiecki, A., Xie, F.-G., & Stępnik, A. 2014, MNRAS, 443, 1733
Niedźwiecki, A., Xie, F.-G., & Zdziarski, A. A. 2012, MNRAS, 420, 1195
O' Riordan, M., Pe'er, A., & McKinney, J. C. 2016a, ApJ, 831, 62
O' Riordan, M., Pe'er, A., & McKinney, J. C. 2016b, ApJ, 819, 95
Pe'er, A., & Casella, P. 2009, ApJ, 699, 1919
Pe'er, A., & Markoff, S. 2012, ApJ, 753, 177
Poutanen, J. 1998, in Theory of Black Hole Accretion Disks, ed. M. A. Abramowicz, G. Bjornsson, & J. E. Pringle (Cambridge: Cambridge Univ. Press), 100
Psaltis, D., Özel, F., Chan, C.-K., & Marrone, D. P. 2015, ApJ, 814, 115
Qiao, E., & Liu, B. F. 2015, MNRAS, 448, 1099
Ressler, S. M., Tchekhovskoy, A., Quataert, E., Chandra, M., & Gammie, C. F. 2015, MNRAS, 454, 1848
Ressler, S. M., Tchekhovskoy, A., Quataert, E., & Gammie, C. F. 2017, MNRAS, 467, 3604
Ryan, B. R., Ressler, S. M., Dolence, J. C., et al. 2017, ApJL, 844, L24
Rybicki, G. B., & Lightman, A. P. 1979, Radiative Processes in Astrophysics (New York: Wiley-Interscience)
Sądowski, A., Wielgus, M., Narayan, R., et al. 2017, MNRAS, 466, 705
Shcherbakov, R. V., & McKinney, J. C. 2013, ApJL, 774, L22
Shcherbakov, R. V., Penna, R. F., & McKinney, J. C. 2012, ApJ, 755, 133
Sironi, L., Keshet, U., & Lemoine, M. 2015, SSRv, 191, 519
Sironi, L., & Spitkovsky, A. 2014, ApJL, 783, L21
Tchekhovskoy, A., Narayan, R., & McKinney, J. C. 2010, ApJ, 711, 50
Tchekhovskoy, A., Narayan, R., & McKinney, J. C. 2011, MNRAS, 418, L79
Titarchuk, L. 1994, ApJ, 434, 570
Yuan, F., Zdziarski, A. A., Xue, Y., & Wu, X.-B. 2007, ApJ, 659, 541